# Assessment of the fracture toughness of neutron-irradiated nuclear graphite by 3D analysis of the crack displacement field*

Xiaochao Jin[1,2], James Wade-Zhu[3], Yang Chen[1], Paul M. Mummery[4], Xueling Fan[2] and T James Marrow[†1]

[1] Department of Materials, University of Oxford, UK

[2] State Key Laboratory for Strength and Vibration of Mechanical Structures, School of Aerospace Engineering, Xi'an Jiaotong University, P. R. China

[3] School of Metallurgy and Materials, University of Birmingham, UK

[4] Department of Mechanical, Aerospace and Civil Engineering, The University of Manchester, UK

## Abstract

Digital volume correlation of in situ synchrotron X-ray computed tomographs has been used to measure the three-dimensional displacement fields around quasi-static propagating cracks in neutron irradiated and unirradiated graphite in small test specimens of the double cleavage drilled compression geometry. The crack tip location and crack opening were extracted from the displacement fields using a phase congruency edge detection method as cracks were propagated over ~5 mm. The cracks propagated in mode I, maintaining a constant crack opening angle that was ~50% smaller for the irradiated graphite. 3D finite element simulations, using the measured full field displacements as boundary conditions, obtained the critical elastic strain energy release rate for crack propagation by calculation of the domain

* Author's copy of paper accepted for publication in Carbon, https://doi.org/10.1016/j.carbon.2020.09.072
† Corresponding author: Email: james.marrow@materials.ox.ac.uk (James Marrow). Tel: +44 1865 273938

contour J-integral. When the non-linear properties of unirradiated graphite were considered, the strain energy release rate for propagation was constant (180 ± 22 $Jm^{-2}$) with increasing crack length. The irradiated graphite (fluence of 19.7 x $10^{20}$ neutrons $cm^{-2}$ or 2.6 dpa, 4% weight loss by radiolytic oxidation) had linear elastic properties, and the strain energy release rate for propagation increased linearly from 118 ± 12 $Jm^{-2}$ to 485 ±75 $Jm^{-2}$ with crack length.

# 1 Introduction

Due to its low neutron absorption and ability to moderate the neutron spectrum, synthetic polygranular graphite is a critical material in gas cooled nuclear fission reactors [1–3]. It is used to carry structural loads, such as in the core of the current Advanced Gas-cooled Reactors (AGR) [4], and is proposed for structural components in future advanced reactors [5]. Lattice defects induced by the interaction of fast neutrons with the graphite crystal cause dimensional change, generate microstrain, and change the physical properties of graphite [2,6]. Oxidation may also occur in some reactor environments [7], and the increased porosity has consequences for graphite properties including the elastic modulus and strength [8,9]. Due to the effects of irradiation, tensile stresses can develop within graphite components during the reactor lifetime that may be sufficient to initiate and propagate fracture [10–13]. It is important to be able to forecast the risk of fracture in the design process and for management of the reactor lifetime [14,15], and this requires knowledge of the fracture resistance of irradiated graphite.

Published data for the fracture behaviour of irradiated graphites are limited. There have been some significant studies with standard geometry specimens that investigated the effects of irradiation on polygranular graphite, without oxidation. In tests of a coarse grained graphite

[16], irradiated at 900°C to a fluence[‡] of ~$10^{22}$ neutrons $cm^{-2}$, the measured fracture toughness (critical mode I stress intensity factor) increased with irradiation dose. Studies of a fine grained graphite, irradiated in the Japanese Material Testing Reactor between 750-1000°C up to a fluence of ~$10^{21}$ neutrons $cm^{-2}$, used a relatively large (~20 to 30 mm diameter) diametral compression specimen geometry to obtain the fracture toughness and reported an increase in fracture toughness (critical stress intensity factor in both modes I and II) with increasing irradiation dose [17]. Similar investigations of graphites irradiated to ~$10^{21}$ neutrons $cm^{-2}$ at 600-850°C found an increase in mode I and mode II fracture toughness with irradiation [18]. Tests using chevron-notched specimens with a polygranular graphite irradiated at high temperatures (600°C and 850°C) to high dose (~$10^{22}$ neutrons $cm^{-2}$) also measured a trend of increasing fracture toughness (critical mode I stress intensity factor) with irradiation dose [19]. One study has used chevron-notched bend specimens to examine the effects of radiation and oxidation in coupons extracted from operating AGRs [20]; the total work of fracture was estimated by an analysis of stable crack propagation. The samples had experienced in-reactor neutron irradiations to a dose of up to ~$10^{22}$ neutrons $cm^{-2}$, which had been accompanied by simultaneous radiolytic oxidation that decreased the graphite density by up to 30%; this had a dominant effect and deceased the work of fracture significantly. This study [20] showed the utility of the chevron geometry for small specimen tests, but the analysis did not permit assessment of the R-curve behaviour (i.e. rising fracture resistance with increasing crack length) that has been observed in larger specimens of unirradiated

[‡] In [16], the neutron dose is reported as being up to 10.2 dpa (displacements per atom) for irradiation in the High Flux Isotope Reactor (HFIR) at Oak Ridge National Laboratory. For comparison with some other irradiation experiments that report only the total neutron fluence (neutrons $cm^{-2}$), we have used the information in [19], which reports irradiations in HFIR at 875°C to 13.5 dpa (2 x $10^{22}$ neutrons $cm^{-2}$), to proportionately estimate the approximate fluence for [16] in neutrons $cm^{-2}$.

graphite [21–23], and for which no data are available for irradiated graphite. These studies indicate that there is an effect of irradiation on fracture behaviour, but they are insufficient to identify the effect of the microstructure. No studies have reported the fracture toughness of irradiated graphite that has been tested at elevated temperatures, though recent novel observations used high resolution tomography to study the effects of temperatures up to 1100°C on fracture propagation in unirradiated graphite, in situ [24].

The fracture resistance of nuclear graphite is generally obtained from large standardised specimens [25], and a challenge is presented by the difficulty of assessing small specimens of irradiated material that represent the state of the graphite in the core of a reactor. The motivation for the work reported in this paper is to investigate test specimens that might be used to measure the fracture resistance of small specimens of graphite that could be obtained from operating reactors cores [26,27] or materials test reactors [28]. One design that is suitable for small specimen tests of brittle materials is the double-cleavage drilled compression (DCDC) geometry [29] (Figure 1). Longitudinal compression of the unconstrained specimen induces a transverse tensile stress that can drive stable propagation of cracks, which initiate at the central drilled hole. The tensile stress includes contributions from flexure of the ligaments on either side of the vertical crack. In principle, direct observation of the relationship between applied stress and crack length can then be used to derive the critical stress intensity factor for crack propagation, i.e. the fracture toughness. The analytical solution (equation 1) for a finite specimen considers the interaction of the crack with the surfaces of the sample in a multiaxial stress field, and assumes linear elastic behaviour of the mode I crack,

$$K_I = -\left(\frac{3}{\pi}\right)^{1/2}\left(\frac{a}{t}\right)^{1/2}\frac{\alpha^2}{(L+1)}\sigma_1\sqrt{\pi a}\left\{\frac{1-\frac{2(L+1)^3 a}{3\ \alpha^2\ t}\lambda}{1+\frac{12\sigma_1 a^2}{\pi^2 E_0 t^2}(L+1)^2}\right\} \quad (1)$$

where $a$ is the hole radius, $L$ is the ratio of the crack length, $l$, to the hole radius ($L = l/a$), $t$ is the specimen half width ($t = w/2$), $\alpha$ is a constant (value 0.6), $E_0$ is the Young's modulus and $\lambda$ is the ratio of transverse stress ($\sigma_3$) to the applied compressive stress ($\sigma_1$), where $\sigma_3 = \lambda\sigma_1$. This solution has been validated by experiments in a range of model brittle materials [29].

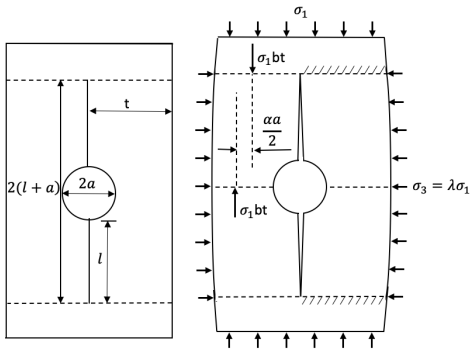


*Figure 1: Schematic of the double-cleavage drilled compression (DCDC) specimen geometry, after* [29].

The DCDC specimen is quite compact and simple to produce, and so it may be a very suitable geometry to assess the fracture resistance of irradiated materials, including testing at elevated temperatures that are representative of the reactor environment. Analytical solutions for such standardised fracture tests use inputs of specimen geometry and the applied load to calculate the stress and strain fields, which provide the critical strain energy for crack propagation. The solution for the stress intensity factor in equation (1) in the DCDC specimen makes significant assumptions for the boundary conditions, in particular the application of a uniaxial and uniform compressive stress ($\lambda = 0$) that is parallel to the mode I crack. This can be difficult to achieve in small test specimens of stiff materials, in which small misalignments or variations in geometry or surface friction may introduce significant stresses.

There is currently no standard to provide guidance on the limitations of the analytical solution, and for irradiated materials there can be restrictions in the handling and preparation of specimens that may increase the potential for errors from dimensional tolerances, alignment and mechanical constraint (i.e. friction) [30].

A recent experiment by some of the authors of this work employed the DCDC specimen geometry to investigate the fracture of a specimen of an irradiated and oxidised nuclear graphite, in a comparative study with non-irradiated graphite of the same type [31]. The specimen geometry allowed examination of the opening behaviour of stable propagating cracks and their interactions with the microstructure, in situ, using high resolution synchrotron X-ray computed tomography (XCT). It was observed that the radiolytically oxidised specimen behaved in a more brittle manner, due to the higher stored elastic strain energy associated with graphite's increased elastic modulus on irradiation. The tomographs allowed direct measurement of the crack opening, and this showed the irradiated specimen had a smaller degree of permanent, non-recoverable damage associated with crack propagation. This was attributed to irradiation-induced closure of micro-to-nano-sized cracks and pores, which suppressed the development of micro-cracking. A greater degree of crack blunting was identified in the radiolytically oxidised specimen, as the propagating crack interacted with the increased porosity. There was no analysis done to quantify the effect of radiolytic oxidation on fracture toughness, though it was observed that the failure strength was increased in the radiolytically oxidised specimen.

The motivation for this work was to investigate whether the DCDC specimen geometry could be used to measure the fracture resistance of small specimens of graphite, with a size typical of those provided by sampling of operating reactors cores or materials test reactors. In the

future, this would allow reliable measurements of the effects of temperature, irradiation and oxidation on graphite fracture toughness. Using the data from the recent experiment [31], a comparison has been made between i) the analytical solution for the DCDC geometry (i.e. equation 1) and ii) an experimentally-informed finite element domain integral method. The former uses the external boundary conditions (i.e. applied load and specimen geometry) with knowledge of the material linear elastic properties, the crack dimension, and the assumption of mode I loading. The latter uses the local crack displacement field and requires knowledge of the material stress/strain behaviour (i.e. linear or non-linear constitutive model), but no knowledge is required of the external boundary conditions acting on the specimen nor any assumption of the dimension or mode of loading of the crack.

# 2 Experiments and analysis methods

In situ high resolution tomographs have been analysed by DVC to characterise the crack opening behaviour and full field displacements of quasi-static propagating cracks in nuclear graphite in unirradiated and irradiated conditions. The materials and experiments that produced the tomographs are fully described in a previous publication by some of the authors [31], and abbreviated details are provided here. In this work, a finite element analysis has been implemented, with boundary conditions from a full field DVC characterisation of the X-ray tomographs, to quantify the strain energy release rate (J-integral) and stress intensity factors of the crack field.

## 2.1 Materials and Experiments

The materials were Gilsocarbon graphite (IM1-24 grade), provided by EDF Energy Ltd (Barnwood, UK). The irradiated graphite had been extracted from one of the Hinkley Point B AGRs in 1993. Its calculated neutron dose was 19.7 x $10^{20}$ neutrons $cm^{-2}$ (2.6 dpa) with a

weight loss from radiolytic oxidation of ~4%. This dose is well before dimensional change turnaround in Gilsocarbon from accommodation porosity closure, which occurs beyond 100 x $10^{20}$ neutrons $cm^{-2}$ at AGR reactor temperature [4]. The measured densities of the unirradiated and irradiated specimens were 1.845 g $cm^{-3}$ and 1.707 g $cm^{-3}$ respectively. The initial density (prior to irradiation) of the irradiated graphite was 1.778 g $cm^{-3}$. The dynamic Young's modulus (DYM), obtained by ultrasonic measurements of independent specimens, was between 9.85- 10.53 GPa for the unirradiated graphite and 12.87-14.01 GPa for the irradiated graphite.

A specimen of the DCDC geometry with dimensions (X × Y × Z) of 8 × 18 × 3 mm was machined from each of the virgin and irradiated graphites, with a central through-thickness hole (2.8 mm diameter) aligned with the Z-direction (Figure 2a). The sample machining was done at the Central Laboratory, National Nuclear Laboratory (Sellafield, UK) using procedures developed for graphite small specimen mechanical testing [20]. The XCT was conducted on the Diamond-Manchester Imaging Branchline I13-2 at the Diamond Light Source (Didcot, UK), using a high-flux, partially-coherent, polychromatic 'pink' (30 keV) X-ray beam [32]. A uniaxial compressive load was applied, along the Y-axis that was parallel to the moulding/pressing direction of the original graphite billets, under displacement control using a 10 kN open-frame rig that was purpose designed for XCT (Deben UK Ltd, Suffolk, UK) with a containment cell to allow testing and in situ observation of radioactive materials [33].

For the unirradiated graphite specimen, six tomography scans were conducted at the pre-load (~0 N), 780 N, 827 N, 857 N and 875 N, with a final scan at 872 N after a peak load was reached. Five scans were conducted similarly for the irradiated graphite specimen at the pre-load (~0 N), 500 N, 914 N, 1026 N and then 1063 N. For each scan, 4,001 radiographic

projections with 0.2 s exposure time were obtained over a 180° rotation, each with a field of view of 6.7 × 5.6 mm (2560 × 2160 pixels at an effective pixel size of 2.6 µm). The tomographs were reconstructed using a filtered back projection algorithm that incorporated ring artefact suppression [34,35]. In the DCDC geometry, crack propagation occurs along the vertical Y axis from both the top and bottom of the hole. The high resolution tomographs repeatedly examined the same region above the central hole in each specimen to observe the development of one crack. Due to longer than anticipated crack propagation in the irradiated graphite, an additional scan was conducted at 1063 N that overlapped the initial scan by 3.6 mm in order to observe the final crack tip location.

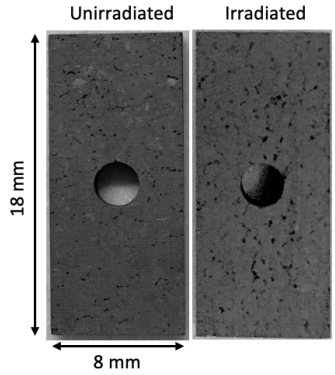


*Figure 2: DCDC (double cleavage drilled compression) specimens of the unirradiated and irradiated Gilsocarbon graphite.*

## 2.2 Digital Volume Correlation

Prior to the DVC analysis, the tomography data were converted from 32-bit to 8-bit using ImageJ [36], while maximising contrast in the graphite microstructure. A 3D Gaussian blur filter (1 pixel radius) was then applied to reduce data noise. The DVC analyses were performed with the LaVision DaVis software (version 8.4.0), using a procedure that combined an initial FFT (Fast Fourier Transform) correlation and then a series of multi-pass direct correlations. The DVC analyses were conducted with the pre-load tomographs as reference. For each

loading step, two sets of analyses were performed separately using subset sizes of 32 × 32 × 32 voxels and 96 × 96 × 96 voxels respectively. For the $32^3$ voxel subset analyses, each tomograph was first cropped to dimensions (X × Y × Z) of 500 × 2150 × 1100 voxels (1.30 × 5.59 × 2.86 mm) about the crack. For the $96^3$ voxel subset analysis, each tomograph was cropped to dimensions (X × Y × Z) of 2500 × 2150 × 1100 voxels (6.50 × 5.59 × 2.86 mm). For all analyses, an overlap of 75% between subsets was adopted and each cropped tomograph observed the edge of the central hole and the full 3 mm thickness of the test specimen in the Z-direction. A correlation coefficient threshold of 0.75 was imposed with any invalid displacement vectors being deleted (i.e. set to 'NaN') with no interpolation from neighbourhood displacements.

## 2.3 Crack Characterization

Phase Congruency (PC) was applied to extract the crack tip position and to measure the crack opening displacements from the DVC data. This is a displacement-based method [37,38] that uses a 3D edge detection algorithm to detect the discontinuity of the crack surface, including the crack tip. Phase congruency is contrast invariant, and identifies features where the Fourier components of the displacement field are most in phase. In this analysis, a Volume Phase Congruency (VPC) map was computed using a novel pseudo method [37,38] in which two-dimensional Phase congruency (2D PC) maps are first calculated iteratively on displacement slices throughout the 3D volume field by a monogenic filter algorithm implemented in Matlab[§]. The 2D PC slices are then combined to generate a pseudo-VPC map. A Hough

[§] Peter Kovesi. MATLAB and Octave Functions for Computer Vision and Image Processing. Available from: <http://www.peterkovesi.com/matlabfns/>

transform of the phase congruency map is used to identify the longest linear feature that is the crack [38].

The mode I, mode II and mode III crack opening displacements (COD), parallel to the X, Y and Z directions, were obtained from the differences between the displacement vectors on either side of the crack. The PC analysis was applied only to the $32^3$ voxel subset data, which had a grid spacing of ~21 μm. The crack lengths were also measured directly by visual inspection of the μXCT images to identify the crack tip.

## 2.4 Finite Element Analysis

The 3D finite element simulations were performed using Abaqus software (version 6.14). The model was established with the same dimensions as the cropped tomography data (6.50 × 5.59 × 2.86 mm), except for the irradiated graphite specimen under 1063 N, which used a larger model that was extended in the Y-direction (6.50 × 7.60 × 2.86 mm). The crack was simplified as a planar discontinuity (Y-Z plane) with its averaged straight crack tip defined by the PC analysis (Figure 3a and b) [Supplementary information, section S1, shows that the simplification to a straight, uniform crack front is reasonable for the purpose of measuring the mean fracture resistance of the microstructure]. Each point of the identified crack tip was an element node, and the mesh refinement in the vicinity of the crack was close to the DVC mesh density of the $32^3$ voxel subset analysis (Figure 3c). The displacement field from the DVC analysis with $96^3$ subset size was injected into the simulation model as the boundary conditions. Following the method of Barhli [39,40], a set of “forbidden nodes” were defined that include the nodes in the vicinity of the crack where the DVC correlation coefficient was low (Figure 3d). The displacements at the forbidden nodes, and other nodes with no injected

DVC displacement, were calculated in Abaqus using the surrounding nodal displacements and the free surface of the crack as boundary conditions.

Both linear elastic and non-linear material models were considered in the simulations for unirradiated graphite, and a linear elastic model was adopted for the irradiated graphite, as fast neutron irradiation removes the non-linear behaviour commonly observed in unirradiated graphite [3]. The linear elastic moduli of the unirradiated and irradiated graphites were taken as 10.05 GPa and 13.50 GPa, respectively, with Poisson's ratio of 0.2. For the non-linear model, the elastic modulus was decreased as a function of the maximum principal strain in the element. It is physically-based [9], and was fitted to experimental data for non-irradiated Gilsocarbon graphite [41]. This non-linear model [39] assumes tensile strain causes microcracks that increase the porosity in proportion to the strain. The dependence of the elastic modulus, $E$, on strain, $\varepsilon$, was defined as:

$$E = E_0\left(1 - (P_0 + A\varepsilon)\right)^n \quad (2)$$

where $E_0$ is the elastic modulus of the pore-free graphite, $P_0$ is the initial porosity ($P_0$= 0.18) [39], $n$=4.12 for interconnected pores of irregular shapes [9], and $A$ is a constant ($A$=36.34). A value of $E_0 = 23.84$ was chosen to give $E$ =10.05 GPa at zero strain.

The non-linear model was implemented as an Abaqus UMAT (User-defined MATerial law), and the resulting stress and strain fields (Figure 3e and f) were used to obtain the elastic strain energy release rate as the J-integral. [Supplementary information, sections S2 and S3, show the effect of non-linear properties on the stress field and provide more information on the definition of the UMAT]. The 3D simulation was analysed as a set of 2D plane strain fields, each parallel to the X-Y plane, and the J-integrals were evaluated for a series of contours around the crack tip at each location along the crack front by using the virtual crack

extension/domain integral method implemented in Abaqus [42,43]. For the linear elastic analyses, the interaction integral method that is available in Abaqus (and which is valid for small scale yielding conditions [44]) allowed calculation of the mode I, mode II and mode III stress intensity factors (SIFs); an example of the variation of the mode I SIF with increasing contour number at three positions (labelled in Figure 3c) along the crack front is shown in Figure 3g. In the J-integral analysis, the contours closest to the crack tip are neglected, and the constant plateau that is approached with increasing contour number provides the optimum calculation of the elastic strain energy release rate and stress intensity factors.

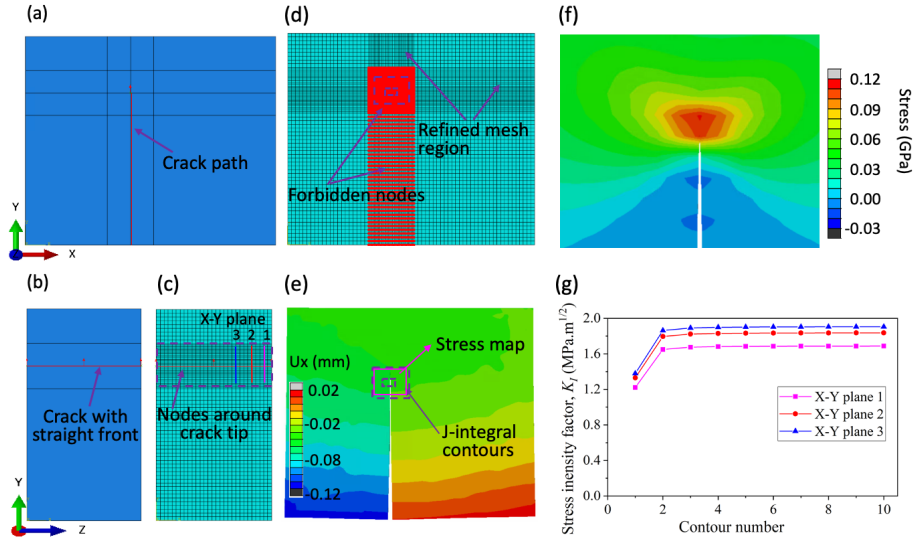


*Figure 3: Illustration of the procedure of finite element analysis using DVC displacement data as boundary conditions, presented for the example of a linear elastic analysis of the unirradiated specimen under a load of 875 N: (a) definition of the planar crack position; (b) definition of the crack with a straight front, using data from the PC analysis; (c) mesh of the model using the crack tip to define nodes; (d) refined mesh around the crack and definition the regions of 'forbidden nodes' with no imposed displacements; (e) definition of the J-integral calculation contours on an example displacement field (dUx) on an X-Y plane near the specimen centre; (f) map of the calculated maximum principal stress in the same X-Y plane; (g) the Mode I Stress Intensity Factor calculated from the J-integral for each contour number at 3 locations - these are labelled in (c).*

# 3 Results

The results of the DVC analysis are first presented, from which the crack length and opening are extracted via a method that considers the phase congruency of the 3D displacement field. These data provide inputs to the finite element analysis of the SIF and strain energy release rate, in which the effect of implementing a non-linear material model for the unirradiated graphite is also considered.

## 3.1 DVC analysis

The development of the crack in the unirradiated graphite is shown in Figure 4, visualised using the maximum normal 3D strain of the DVC analysis at $32^3$ voxel subset and as slices of the µXCT data. All the observations are presented for the same X-Y section near the centre of the specimen (Z = 1.43 mm). The crack, which is first observed at 780 N, has similar dimensions in both visualisations - the extent of the crack is outlined by a red box in the XCT images. The displacement fields measured by the DVC analysis with $96^3$ voxel subset size are shown in Figure 5. As no registration of the datasets was done before the DVC analyses, the small rigid body movements of the specimen due to the mechanical loading are apparent. The displacement fields are generally smooth, and the crack is quite clearly observed due to the discontinuity of the crack opening in the X direction. To estimate an upper bound of DVC measurement uncertainty, the standard deviation in the displacement magnitude was measured in a region that was remote (5 mm) from the stress concentration. For the unirradiated graphite specimen under 780 N, with subsets of $32^3$ and $96^3$ voxel, the standard deviations of the sampled displacements (n=312 and 104, respectively) were 0.58 and 1.60 µm (0.22 and 0.62 voxel), respectively. For the irradiated graphite specimen under 500 N,

with subsets of $32^3$ and $96^3$ voxel, the standard deviations of the sampled displacements (n=312 and 104, respectively) were 0.50 and 0.65 µm (0.19 and 0.25 voxel), respectively.

The crack development in the irradiated graphite is shown in Figure 6. A short crack, less than 0.5 mm in length, is first observed at 914 N, and it extends significantly as the load increases. The crack path appears more tortuous than in the unirradiated graphite and intersects the increased porosity from radiolytic oxidation. This also makes it more difficult to measure the crack length directly in the XCT images, without subjective judgements of the tip location in the complex microstructure. In the last loading step, the crack length that is obtained using the $32^3$ subset DVC data for maximum normal 3D strain is clearly shorter than the visible length; this is because there was no reference tomograph of the region that contained the final crack tip position so it is beyond the boundary of the DVC analysed region. Some secondary cracking also developed close to the central hole at the last stage. The displacement fields from the DVC analysis with $96^3$ voxel subset size for the irradiated specimen are shown in Figure 7. The displacements show the effects of rigid body movements of the specimen whilst loading was applied, but the opening of the crack is clearly observed in the X-displacement field.

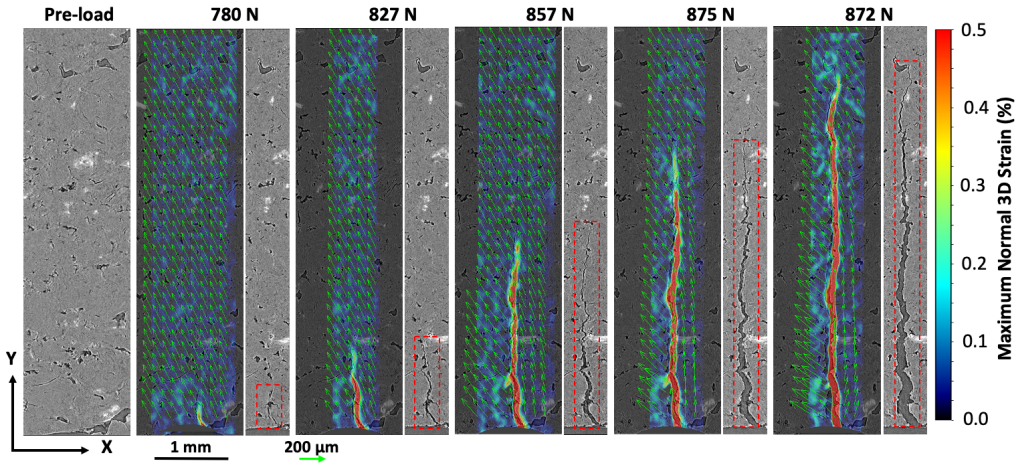


*Figure 4: Visualization of the crack as it propagated in the unirradiated graphite with increasing load. The crack is visualised in virtual slices and with contour maps of maximum normal 3D strain in the X-Y plane near the centre of the specimen. The red dashed box in the tomographs marks the extent of the visible crack. The green arrows show the direction and magnitude of the displacements in the X-Y plane, relative to the preloaded tomograph.*

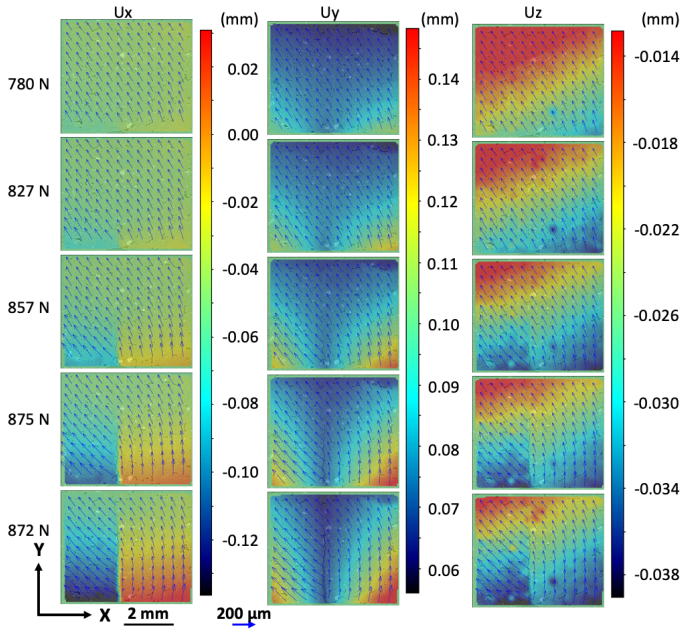


*Figure 5: The evolution with load of the displacement fields relative to the preloaded tomograph of the unirradiated graphite specimen, measured by DVC and presented on an X-Y plane near the specimen centre. The colour contours show the displacements (mm) in the X, Y and Z directions (Ux, Uy and Uz), and the blue arrows represent the displacement vectors in the X-Y plane.*

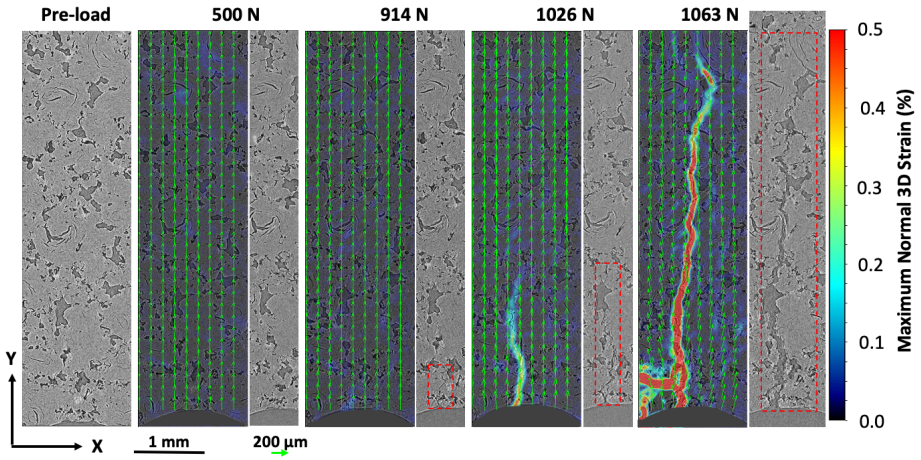


*Figure 6: Visualization of the crack as it developed in the irradiated graphite with increasing load. The crack is visualised in virtual slices and contour maps of maximum normal 3D strain in the X-Y plane near the centre of the specimen. The red dashed box marks the extent of the visible crack. The green arrows show the displacements in the X-Y plane, relative to the preloaded tomograph.*

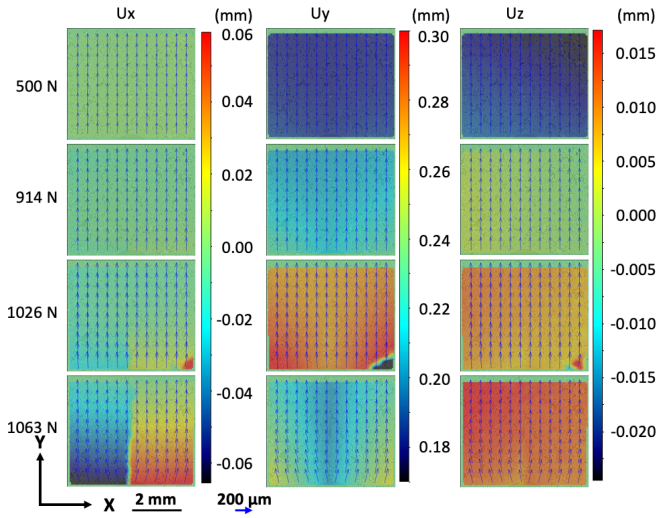


*Figure 7: The evolution of the displacement fields of the irradiated graphite specimen with increasing load, measured by DVC and presented on an X-Y plane near the specimen centre. The blue arrows represent the displacement vectors in the X-Y plane, and the colour contours show the displacements (mm) in the X, Y and Z directions (Ux, Uy and Uz), relative to the preloaded tomograph.*

## 3.2 Phase Congruency analysis

The crack length, identified using the PC analysis to detect the crack tip, was measured as the vertical Y-distance from the crack mouth at the edge of the drilled hole to the crack tip. The data are compared in Figure 8 with the crack length obtained similarly by visual inspection of the XCT images, with good agreement shown between the two methods. The PC analysis is less subjective than visual inspection or thresholding of the 3D strain field. The irregular crack front is quite uniform across the thickness of the specimens, though differences occur close to one side (Z < 0.25 mm) in the unirradiated graphite that may be due to DVC errors close to the specimen edge. The PC-measured crack length in the irradiated graphite at 1063 N is smaller than the actual crack length, as the crack tip extended beyond the boundary of the DVC-analysed data. The average crack lengths are summarised in Table 1.

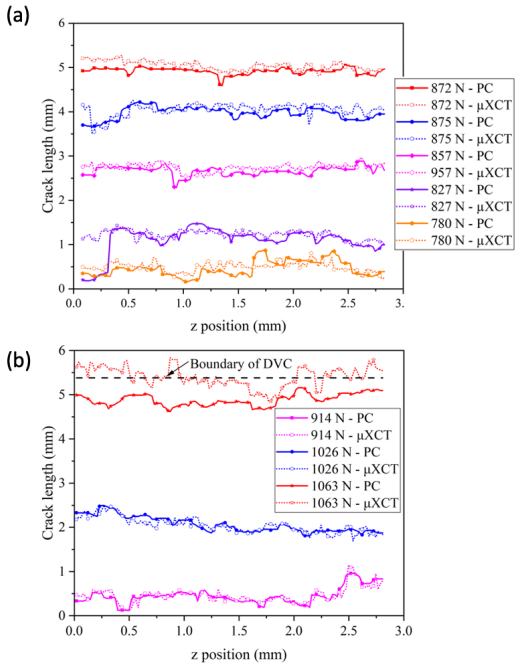


*Figure 8: The variation of the crack length across the specimen at different loads: (a) unirradiated and (b) irradiated graphite. The full symbols show data obtained by the PC analysis of the DVC displacement field; open symbols show data obtained by visual inspection of the XCT images.*

*Table 1: The development of the crack length in the unirradiated and irradiated graphite specimens with load.*

| **Specimen** | **Load (N)** | **Crack length (mm) [average ± s.d.]** | |
|---|---|---|---|
| | | XCT | PC |
| Unirradiated | 780 | 0.49±0.11 | 0.45±0.18 |
| | 827 | 1.22±0.10 | 1.10±0.30 |
| | 857 | 2.74±0.09 | 2.67±0.10 |
| | 875 | 4.04±0.14 | 3.97±0.14 |
| | 873 | 5.04±0.10 | 4.92±0.08 |
| Irradiated | 914 | 0.46±0.18 | 0.45±0.18 |
| | 1026 | 2.05±0.17 | 2.06±0.18 |
| | 1063 | 5.40±0.23 | 4.88±0.13 |

The PC analysis allowed mapping of the crack opening displacements (COD) between the crack surfaces, by using the relative difference between the components of the displacement vectors closest to the identified discontinuity of the crack. Maps showing the development of the CODs for the unirradiated (Figure 9) and irradiated (Figure 10) graphite specimens were obtained, which describe the crack opening in Mode I, Mode II and Mode III respectively. For the irradiated graphite observed at 1063 N, due to low correlation coefficients at some locations in the DVC analysis, there are no displacement data immediately adjacent to the crack. These positions are shown in the COD maps as white bands. The COD maps show that crack essentially propagated under mode I, with smaller displacements in modes II and III. The effect of the secondary cracking close to the hole in the irradiated graphite at maximum load (1063 N) can be observed as a local reduction on the mode I COD, as the opening of secondary crack accommodates some of the applied strain.

The COD maps (Figure 9 and Figure 10) show that the crack opens quite evenly across the thickness of the specimens. The crack mouth opening displacements (CMOD) were measured at the intersection of the crack with the central hole and averaged across the specimen thickness; they are presented in Figure 11a as a function of the visible crack length, which was measured directly from the XCT images. The mode I CMOD increases in proportion with the

crack length for both graphites and is a significantly larger for the unirradiated graphite. The mode II and mode III CMOD remain small and approximately constant for the unirradiated graphite, but at the longest crack length for the irradiated graphite specimen there are significant mode II and III displacements at the crack mouth. The mode I COD data are summarised in Figure 11b, averaged through the specimen thickness (Z) and presented as a function of distance towards the crack mouth from the average position of the visible crack tip. This shows the crack tip opens with an angle that is larger for the unirradiated graphite (~2°) than the irradiated graphite (~1°). The angle is effectively constant for the unirradiated graphite, but slightly increases with load for the irradiated specimen. The secondary cracking in the irradiated graphite at the maximum applied load (1063 N), which is seen in Figure 6 and also Figure 10, causes a local decrease in the crack opening in the vicinity of the crack mouth.

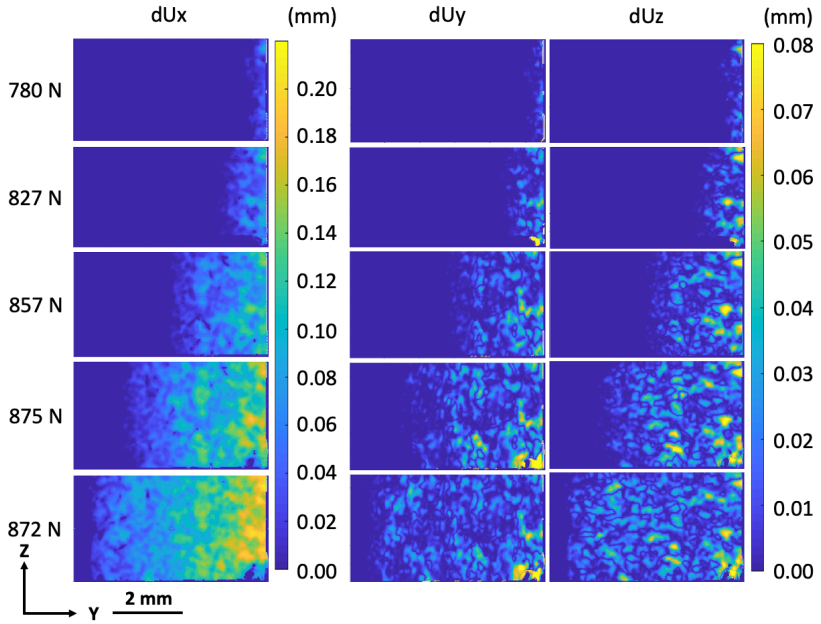


*Figure 9: Maps of the crack opening displacements in the unirradiated graphite, measured in the X (dUx), Y (dUy) and Z (dUz) directions, as a function of the applied load. The crack tip propagates from right to left.*

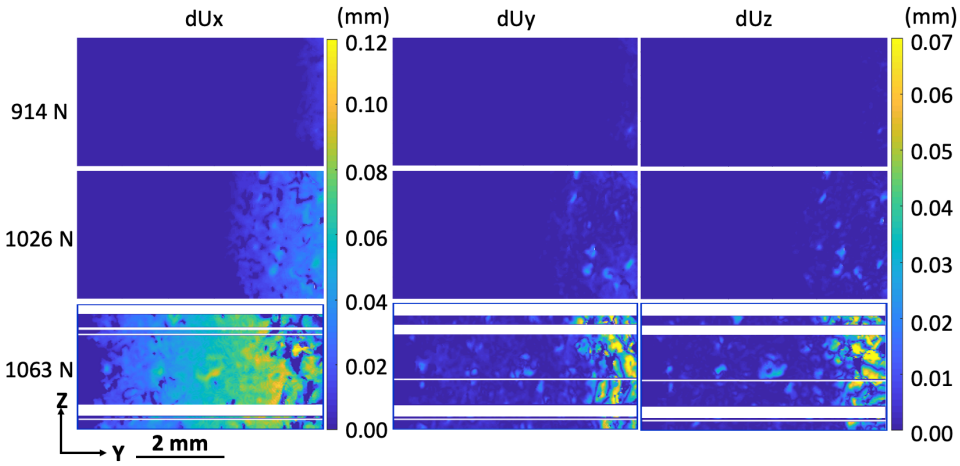


*Figure 10: Maps of the crack opening displacements in the irradiated graphite, measured in the X (dUx), Y (dUy) and Z (dUz) directions, as a function of the applied load. The crack tip propagates from right to left.*

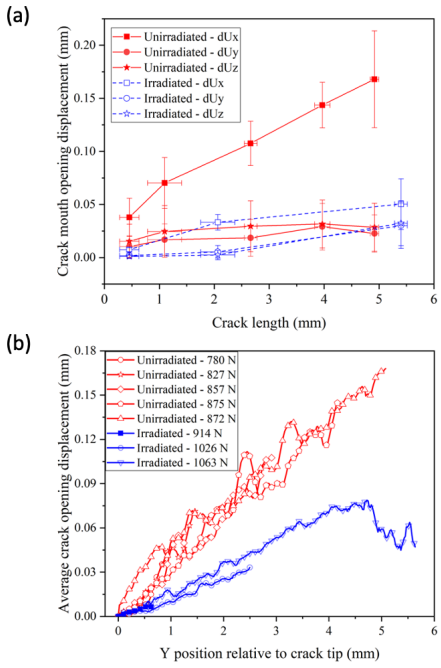


*Figure 11: (a) The components of the crack mouth opening displacements (dUx, dUy and dUz) as a function of crack length (error bars are the standard deviation). (b) The crack opening displacements (dUx) averaged across the specimen thickness (one in every five points shown), as a function of the Y-distance towards the crack mouth, measured from the average position of the visible crack tip.*

## 3.3 Analysis of SIF and Strain Energy Release Rate

The finite element simulations calculated the elastic strain energy release rate by using the J-integral. The calculations were done at 30 equally spaced points along the crack front (Figure 3c) for each analysis. The SIF and J-integral values are taken as the average results between the third and tenth contours (see Figure 3g) of all the positions across the specimen thickness. The variation of J-integral across the specimen, calculated with linear-elastic properties, are presented in Figure 12a and b, showing that the strain energy release rate near the specimen surface is lower than that near the specimen centre. The strain energy release rate of the unirradiated graphite did not change systematically with load (Figure 13a), while that of the irradiated graphite increased (Figure 14b).

With the assumption of constant linear elastic properties, the interaction integral provided the linear elastic SIFs for modes I to III as $K_I$, $K_{II}$ and $K_{III}$. These are presented in Figure 13a. For the unirradiated graphite, the average SIFs are all approximately constant as the crack extends. The mode I SIF, $K_I$, is dominant, with an average value of 1.97 ± 0.14 MPa·m$^{1/2}$ (the uncertainty is the standard deviation). For the irradiated graphite, there is a linear increase of $K_I$ from 1.26 $\pm$ 0.07 to 2.01 $\pm$ 0.47 MPa·m$^{1/2}$ as the crack extends. In

Table 2, these data are compared with the mode I SIFs obtained using the analytical solution, i.e. equation (1), which obtains substantially lower values that decrease with increasing crack length.

*Table 2: J-integral and stress intensity factors (K) of unirradiated and irradiated graphite specimens under different loads. The analytical solution of equation (1) provides $K_{eq(1)}$. $J_{linear}$ is the J-integral obtained using the finite element method with the assumption of linear elasticity, from which $K_I$ to $K_{III}$ are extracted using the interaction integral. $J_{non\text{-}linear}$ is obtained for the unirradiated graphite using the non-linear model. Each data of the J and K is the average of about 210 data points.*

| Specimen | Load (N) | $K_{eq.(1)}$ (MPa·m$^{1/2}$) | $J_{linear}$ (J·m$^{-2}$) | $K_i$ (MPa·m$^{1/2}$) | $K_{ii}$ (MPa·m$^{1/2}$) | $K_{iii}$ (MPa·m$^{1/2}$) | $J_{non\text{-}linear}$ (J·m$^{-2}$) |
|---|---|---|---|---|---|---|---|
| Unirradiated | 780 | 0.34 | 392±55 | 1.97±0.10 | 0.12±0.06 | 0.23±0.08 | 173±20 |
| | 827 | 0.20 | 409±39 | 2.05±0.15 | 0.21±0.19 | 0.30±0.15 | 189±25 |
| | 857 | 0.12 | 323±42 | 1.82±0.16 | 0.27±0.14 | 0.27±0.12 | 138±14 |
| | 875 | 0.09 | 366±54 | 1.92±0.15 | 0.13±0.05 | 0.28±0.13 | 184±21 |
| | 873 | 0.08 | 437±57 | 2.11±0.14 | 0.20±0.09 | 0.18±0.24 | 216±21 |
| Irradiated | 914 | 0.40 | 118±12 | 1.26±0.07 | 0.16±0.03 | 0.09±0.02 | -- |
| | 1026 | 0.24 | 227±47 | 1.68±0.19 | 0.56±0.04 | 0.11±0.06 | -- |
| | 1063 | 0.13 | 485±75 | 2.51±0.47 | 0.34±0.11 | 0.12±0.04 | -- |

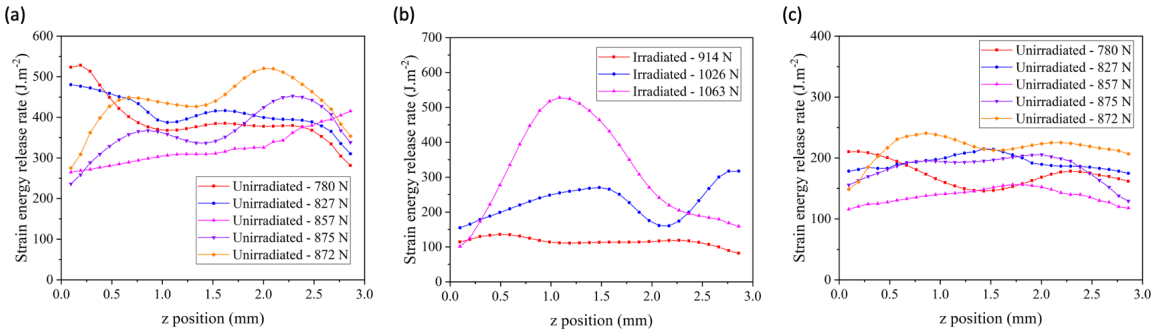


*Figure 12: The strain energy release rate (J-integral) across the specimen at different loads: (a) unirradiated graphite with a linear model; (b) irradiated graphite with a linear model; (c) unirradiated graphite with a non-linear model.*

The variation of the J-integral across the crack front for the non-irradiated graphite with the non-linear model is shown in Figure 12c, and is similar for all crack lengths. Figure 13b presents the strain energy release rate as a function of crack length, evaluated as the J-integral; results are shown for both linear and non-linear material models for the unirradiated graphite, and with a linear model for the irradiated graphite. The evaluation of the stress intensity factors requires the assumption of small scale yielding and constant elastic modulus. This may not be strictly valid for the non-linear elastic model; hence the equivalent stress intensity factors were not calculated. The strain energy release rate for the unirradiated

graphite with the assumption of linear properties was effectively constant with an average of 385 ± 49 J·m$^{-2}$, and with the non-linear model, the strain energy release rate reduced to 180 ± 20 J·m$^{-2}$. The average strain energy release rate obtained for the irradiated graphite increased linearly from 128 ± 12 to 485 ±75 J·m$^{-2}$ as the crack extended, with some significant variation developing across the crack front.

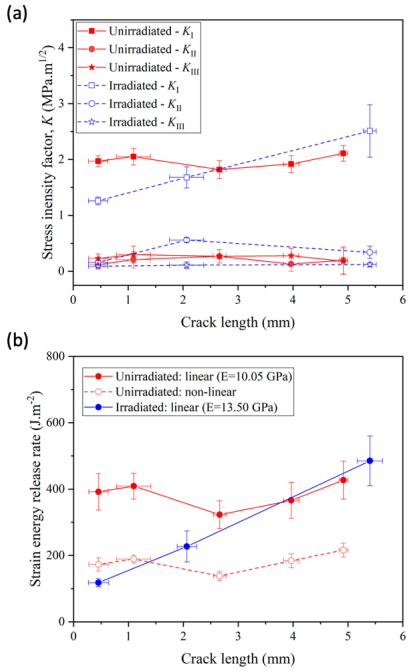


*Figure 13: (a) Stress intensity factors ($K_I$, $K_{II}$ and $K_{II}$ represent stress intensity factors under mode I, II and III) determined as a function of the crack length via finite element simulation with DVC displacements as the boundary conditions; (b) Strain energy release rate (J-integral) as a function of the crack length. The full symbols show data obtained with linear elastic material models; open symbols show data obtained with a non-linear model. The error bars are the standard deviations.*

# 4 Discussion

The phase congruency analysis of the displacement fields provides an objective method to identify the position of the crack tip and to quantify the opening of the crack (Figure 9 and Figure 10). The loading of the crack in the DCDC geometry is predominantly mode I (Figure 11a), with a crack opening angle that is approximately constant for the unirradiated graphite and that increases slightly with crack length for the irradiated graphite (Figure 11b). The stable crack is in equilibrium with the critical SIF for crack propagation, yet the values for the mode I SIF $K_1$ obtained using the analytical solution of equation (1) (

Table 2) decrease quite strongly with increasing crack length. This seems unrealistic, and the assumed boundary conditions in equation (1) are judged to be incorrect, particularly $\lambda = 0$ that assumes uniform stress.

In a short specimen, the effects of fixed vertical displacements and friction at the boundary may become significant, with lateral tension ($\lambda < 1$) induced due to these constraints. Lateral tension would act to increase the mode I stress intensity factor acting on the crack, and so decrease the apparent fracture toughness that is calculated with the assumption of $\lambda = 0$. Asymmetry due to non-uniform contact, crushing, and damage in the ligament adjacent to the central hole may also cause the loading of the propagating crack to deviate from the assumed symmetry of mode I. This is apparent in the development of the crack opening displacements (e.g. Figure 11, irradiated specimen at 1063 N). Errors due to lateral tension would be reduced for a longer test specimen or for shorter cracks, in which case equation (1) would become a more faithful approximation, albeit limited in application to linear elastic behaviour and mode I loading. In short specimens, which are desirable for the testing of small quantities of material such as irradiated graphite, it is difficult to estimate the error that may arise due from the assumption that $\lambda = 0$ and equation (1) may not be relied upon.

The 3D displacement field was measured directly by DVC so the strain energy release rate for crack propagation could be evaluated by finite element simulation with the displacements as boundary conditions. With the assumption of small-scale yielding, the stress field is obtained from the displacement field via the linear elastic moduli, and the mode II and mode III SIFs may also be evaluated using the interaction integral. This analysis finds that the crack in the unirradiated graphite propagated with an approximately constant mode I SIF (1.97 ± 0.14 MPa·m$^{1/2}$), whereas for the irradiated graphite the initial toughness was lower (1.26 $\pm$ 0.07)

rising to 2.01 ± 0.47 MPa·m$^{1/2}$ as the crack extended (Figure 13a). For both materials, the cracks propagated in a stable manner, and the mode II and mode III SIFs were small in comparison with the mode I SIF. This is the expected behaviour of the DCDC specimen.

The linear elastic analysis neglects the non-linear properties of unirradiated graphite, for which the elastic modulus reduces with increasing tensile strain [41]. This reduces the stresses close to the crack tip [39], so a linear elastic analysis overestimates the elastic strain energy of the crack field. The assumption of small-scale yielding is not valid for the unirradiated graphite and incorporating its non-linear behaviour in the finite element simulation, via the non-linear model of equation (2), reduced the average strain energy release rate from 385 ± 49 J·m$^{-2}$ to 180 ± 20 J·m$^{-2}$ (Figure 13b). Previous assessments of the work of fracture in Gilsocarbon graphite were for graphite used in the Heysham B reactors. These obtained a value of ~200 J·m$^{-2}$ via measurement of the total work of fracture in small chevron-notch specimens [20] and also via a non-linear finite-element analysis with measured boundary conditions [39] of the strain energy release rate for crack propagation in a test specimen that was large compared to the fracture process zone. The work of fracture obtained in this work for unirradiated IM1-24 Hinkley Point B Gilsocarbon graphite is close to that obtained for unirradiated GCMB Heysham B Gilsocarbon graphite.

The finite element analysis of the strain energy release rate from the displacement field depends on knowledge of the elastic modulus. Its value depends on the raw materials and processing of the graphite, and graphites with different properties were used in the UK AGRs. The current analysis, which is for the IM1-24 Gilsocarbon graphite used in the Hinkley Point B reactors, assumed $E$= 10.05 GPa (DYM) at zero strain, within a reported measurement range of 9.85 to 10.53 GPa. The DYM, which is measured by ultrasonic methods, is close to the static

Young's modulus that is measured via bulk deformation in mechanical tests if the static modulus is measured at small strains (<0.05%) [45]. For structural calculations with Gilsocarbon graphite, the ratio of the static to dynamic modulus is usually taken as 0.84 for unirradiated graphite and 0.92 for irradiated graphite [46]. This is consistent with the relative dynamic (~12.7 GPa) and static moduli (~11.6 GPa) reported for the GCMB Gilsocarbon graphite used in the Heysham B AGRs [39,47]. Consequently, the static modulus of the unirradiated Hinkley Point B Gilsocarbon examined in this work is expected to be in the range 8.3 to 8.9 GPa. If used in the strain energy calculation, this would proportionately reduce the value of $E_0$ in equation (2), with a consequent reduction in the strain energy release rate that is calculated from the measured displacement field. The values of J-integral presented in Figure 12c and Figure 13b may then overestimate the strain energy release rate by approximately 15% for the unirradiated graphite, and around 10% for the irradiated graphite.

There is no change in fracture resistance with increasing crack length in the unirradiated graphite (Figure 13). Gilsocarbon graphite has been reported to exhibit rising fracture resistance with increasing crack length (R-curve behaviour) in the un-irradiated state [22,23]; in these studies the extent of crack growth was quite significant (of the order of several cm), which would enable toughening mechanisms such as crack bridging and bifurcation to evolve. The toughness measured in the DCDC specimen for a short crack extension should therefore represent the intrinsic fracture resistance of the unirradiated graphite microstructure. This is also consistent with the observation in [39] that the strain energy release rate for unirradiated Heysham B Gilsocarbon graphite (GCMB) was essentially constant for crack extensions up to 6.5 mm. The irradiated graphite exhibits R-curve behaviour (Figure 13) that may be due to the observed strong interaction with the increased porosity that would tend to blunt and deflect the crack tip as it propagates, and it has also been observed that crack propagation in

the irradiated graphite tended to occur along the filler-binder boundary [31]. The initial toughness of the irradiated graphite is lower than that of the unirradiated graphite. Previous studies have reported increased fracture resistance for irradiated graphite in the absence of oxidation [16–19], so the lower toughness in this work may be largely due to the increased porosity from oxidation, which reduces the tensile properties of graphite [9].

Comparison of the crack opening profiles (Figure 11b) and SIFs (Figure 13) show that the crack opening angle scales broadly with the linear elastic mode I SIF. Measurements of the crack opening profile for a wedge-loaded specimen of unirradiated Heysham B Gilsocarbon graphite (GCMB) [39] found the crack propagated with a constant angle of approximately 0.6°, which is smaller than the 2° angle obtained in this work. Nonetheless, the strain energy release rates with mode I crack propagation, obtained using the same material models, were closely similar. Loading the DCDC specimen to propagate fracture requires a significant compressive stress along the axis, which affects the strain energy field. The crack opening angle is therefore not a sufficient parameter to describe fracture resistance as a material parameter, as it is affected by the stress state and is sensitive to specimen geometry.

# 5 Conclusion

Analysis of synchrotron X-ray computed tomographs by digital volume correlation, phase congruency and finite element methods allowed a quantitative investigation of the fracture behaviour of unirradiated and irradiated graphite specimens. The PC analysis of the DVC-measured displacement field gave reliable and objective assessments of crack length, crack opening displacement and crack mouth opening displacement in the porous graphite microstructure. The cracks in both specimens propagated predominantly in mode I at a constant crack opening angle, which was ~50% lower for irradiated graphite than the

unirradiated graphite. Using the displacement fields from the DVC analysis as boundary conditions, stress intensity factors and strain energy release rates (J-integral) of unirradiated and irradiated graphite were evaluated in finite element simulations. With the assumption of linear elastic properties, the strain energy release rate and mode I stress intensity factor were almost constant in the unirradiated graphite specimen, whereas rising values were observed in the irradiated graphite as the cracks extended over a distance of 5 mm. Applying a non-linear model in the analysis of the unirradiated graphite reduced the strain energy release rate due to the reduction in strain energy at the crack tip. The initial toughness of the irradiated graphite ($128 \pm 12$ J·m$^{-2}$), which had ~4% weight loss due to oxidation, was then lower than obtained for the unirradiated graphite ($180 \pm 20$ J·m$^{-2}$).

## Acknowledgement

Two authors (JW/PMM) were supported through IUK Grant TS/M007723/1 “Influence of Creep and Geometry on Strength of Irradiated Graphite Components”. X-C Jin gratefully acknowledges the support of the China Scholarship Fund (Award No. 201806280383) that enabled his participation in this work. The experimental data were obtained in beamtime awarded for experiment MT16668 at the Diamond-Manchester Imaging Branchline I13-2 at the Diamond Light Source (Didcot, UK). The materials were provided by EDF Energy Ltd (Barnwood) and machined at NNL (UK National Nuclear Laboratory). The software and workstation used for the digital volume correlation analysis was supported by EPSRC Grant EP/M02833X/1 “University of Oxford: experimental equipment upgrade”.

## Credit Statement

**Xiaochao Jin:** formal analysis, software, writing - original draft. **James Wade-Zhu**: investigation, writing - review and editing. **Yang Chen:** software, writing - review and editing

**Paul M. Mummery:** funding acquisition, investigation, writing - review and editing. **Xueling Fan**: Funding acquisition. **T. James Marrow:** conceptualisation, supervision, writing - review and editing.

## References


[1] Bonal JP, Kohyama A, Van Der Laan J, Snead LL. Graphite, ceramics, and ceramic composites for high-temperature nuclear power systems. MRS Bulletin 2009;34:28–34.

[2] Kelly BT. Graphite—the most fascinating nuclear material. Carbon 1982;20:3–11. doi:10.1016/0008-6223(82)90066-5.

[3] Taylor R, Brown RG, Gilchrist K, Hall E, Hodds AT, Kelly BT, et al. The mechanical properties of reactor graphite. Carbon 1967;5:519–31. doi:10.1016/0008-6223(67)90029-2.

[4] Marsden BJ, Hall GN. Comprehensive Nuclear Materials. vol. 4. Elsevier; 2012. doi:10.1016/B978-0-08-056033-5.00092-6.

[5] Abram T, Ion S. Generation-IV nuclear power: A review of the state of the science. Energy Policy 2008;36:4323–30. doi:10.1016/j.enpol.2008.09.059.

[6] Krishna R, Wade J, Jones AN, Lasithiotakis M, Mummery PM, Marsden BJ. An understanding of lattice strain, defects and disorder in nuclear graphite. Carbon 2017;124:314–33. doi:https://doi.org/10.1016/j.carbon.2017.08.070.

[7] Eto M, Growcock FB. Effect of oxidizing environment on the strength of H451, PGX and IG-11 graphites. Carbon 1983;21:135–47. doi:10.1016/0008-6223(83)90169-0.

[8] Moskovic R. Degradation of graphite in gas cooled reactors due to radiolytic oxidation. Nuclear Engineering and Design 2014;269:83–7. doi:10.1016/j.nucengdes.2013.08.011.

[9] Vertyagina Y, Marrow TJ. A multi-scale three-dimensional Cellular Automata fracture model of radiolytically oxidised nuclear graphite. Carbon 2017;121:574–90. doi:10.1016/j.carbon.2017.06.031.

[10] Mohanty S, Majumdar S, Srinivasan M. Constitutive modeling and finite element procedure development for stress analysis of prismatic high temperature gas cooled reactor graphite core components. Nuclear Engineering and Design 2013;260:145–54. doi:10.1016/j.nucengdes.2013.03.003.

[11] Sumita J, Shimazaki Y, Shibata T. Investigation on structural integrity of graphite component during high temperature 950 °C continuous operation of HTTR. Journal of Nuclear Science and Technology 2014;51:1364–72. doi:10.1080/00223131.2014.942240.

[12] Tsang DKL, Marsden BJ. The development of a stress analysis code for nuclear graphite components in gas-cooled reactors. Journal of Nuclear Materials 2006;350:208–20. doi:10.1016/j.jnucmat.2006.01.015.

[13] Svalbonas V, Stilwell TC, Zudans Z. Rules for design of nuclear graphite core components — Some considerations and approaches. Nuclear Engineering and Design 1978;46:313–33. doi:https://doi.org/10.1016/0029-5493(78)90018-3.

[14] Hindley MP, Blaine DC, Groenwold AA, Becker TH. Failure prediction of full-size reactor components from tensile specimen data on NBG-18 nuclear graphite. Nuclear Engineering and Design 2015;284:1–9. doi:10.1016/j.nucengdes.2014.12.011.

[15] Yu S, Fang X, Wang H, Li C. Failure probability study of HTR graphite component using microstructure-based model. Nuclear Engineering and Design 2012;253:192–9. doi:10.1016/j.nucengdes.2012.08.019.

[16] Burchell TD, Strizak JP. The effect of neutron irradiation on the fracture toughness of graphite. Nuclear Engineering and Design 2014;271:262–9. doi:https://doi.org/10.1016/j.nucengdes.2013.11.046.

[17] Sato S, Kurumada A, Kawamata K, Takizawa T, Teruyama K. Neutron irradiation effects on thermal shock resistance and fracture toughness of graphites as plasma-facing first wall components for fusion reactor devices. Carbon 1989;27:507–16. doi:https://doi.org/10.1016/0008-6223(89)90001-8.

[18] Sato S, Imamura Y, Kawamata K, Awaji H, Oku T. Irradiation effects on thermal shock resistance and fracture toughness of HTGR-graphite. Nuclear Engineering and Design 1980;61:383–97. doi:10.1016/0029-5493(80)90008-4.

[19] Burchell TD, Eatherly WP. The effects of radiation damage on the properties of GraphNOL N3M. Journal of Nuclear Materials 1991;179–181:205–8. doi:https://doi.org/10.1016/0022-3115(91)90062-C.

[20] Tzelepi A, Ramsay P, Steer AG, Dinsdale-Potter J. Measuring the fracture properties of irradiated reactor core graphite. Journal of Nuclear Materials 2018;509:667–78. doi:10.1016/j.jnucmat.2018.07.024.

[21] Ouagne P, Neighbour GB, McEnaney B. Crack growth resistance in nuclear graphites. Journal of Physics D: Applied Physics 2002;35:927–34. doi:10.1088/0022-3727/35/9/315.

[22] Becker TH, Marrow TJ, Tait RB. Damage, crack growth and fracture characteristics of nuclear grade graphite using the Double Torsion technique. Journal of Nuclear Materials 2011;414:32–43. doi:10.1016/j.jnucmat.2011.04.058.

[23] Hodgkins A, Marrow TJ, Mummery P, Marsden B, Fok A. X-ray tomography observation of crack propagation in nuclear graphite. Materials Science and Technology 2006;22:1045–51. doi:10.1179/174328406X114126.

[24] Liu D, Gludovatz B, Barnard HS, Kuball M, Ritchie RO. Damage tolerance of nuclear graphite at elevated temperatures. Nature Communications 2017;8. doi:10.1038/ncomms15942.

[25] ASTM International. ASTM D7779-11(2015), Standard Test Method for Determination of Fracture Toughness of Graphite at Ambient Temperature. West Conshohocken, PA: 2015. doi:10.1520/D7779-11R15.

[26] Bradford MR. An overview of British Energy's graphite core assessment methodology. Special Publication-Royal Society of Chemistry 2007;309:19.

[27] Metcalfe MP, Tzelepi N, Wilde D. Graphite Testing for Nuclear Applications: The Significance of Test Specimen Volume and Geometry and the Statistical Significance of Test Specimen Population. vol. STP 1578. 100 Barr Harbor Drive, PO Box C700, West Conshohocken, PA 19428-2959: ASTM International; 2014. doi:10.1520/STP1578-EB.

[28] Carroll, M.C., Rohrbaugh, D.T., Chakraborty, P., Swank WD. Evaluating alternate test techniques to characterize mechanical properties in nuclear-grade graphites. International Topical Meeting on High Temperature Reactor Technology 2016:269–75.

[29] Sammis CG, Ashby MF. The failure of brittle porous solids under compressive stress states. Acta Metallurgica 1986;34:511–26. doi:https://doi.org/10.1016/0001-6160(86)90087-8.

[30] ASTM International. ASTM C1424-15(2019), Standard Test Method for Monotonic Compressive Strength of Advanced Ceramics at Ambient Temperature. West Conshohocken, PA: 2019. doi:10.1520/C1424-15R19.

[31] Wade-Zhu J, Krishna R, Bodey AJ, Davies M, Bourne NK, Rau C, et al. 4D synchrotron X-ray microtomography of fracture in nuclear graphite after neutron irradiation and radiolytic oxidation. Carbon 2020;168:230–44. doi:https://doi.org/10.1016/j.carbon.2020.06.051.

[32] Pešić ZD, Fanis A De, Wagner U, Rau C. Experimental stations at I13 beamline at Diamond Light Source. Journal of Physics: Conference Series 2013;425:182003. doi:10.1088/1742-6596/425/18/182003.

[33] Bodey AJ, Mileeva Z, Lowe T, Williamson-Brown E, Eastwood DS, Simpson C, et al. Simultaneous heating and compression of irradiated graphite during synchrotron microtomographic imaging. Journal of Physics: Conference Series 2017;849:012021. doi:10.1088/1742-6596/849/1/012021.

[34] Basham M, Filik J, Wharmby MT, Chang PCY, El Kassaby B, Gerring M, et al. Data Analysis WorkbeNch (DAWN). Journal of Synchrotron Radiation 2015;22:853–8. doi:10.1107/S1600577515002283.

[35] Titarenko V, Bradley R, Martin C, Withers PJ, Titarenko S. Regularization methods for inverse problems in x-ray tomography. In: Stock SR, editor. Developments in X-Ray Tomography VII, vol. 7804, SPIE; 2010, p. 282–91. doi:10.1117/12.860260.

[36] Rueden CT, Schindelin J, Hiner MC, DeZonia BE, Walter AE, Arena ET, et al. ImageJ2: ImageJ for the next generation of scientific image data. BMC Bioinformatics 2017;18:529. doi:10.1186/s12859-017-1934-z.

[37] Cinar AF, Barhli SM, Hollis D, Flansbjer M, Tomlinson RA, Marrow TJ, et al. An autonomous surface discontinuity detection and quantification method by digital image correlation and phase congruency. Optics and Lasers in Engineering 2017;96:94–106. doi:10.1016/j.optlaseng.2017.04.010.

[38] Cinar A. Image-Based Fracture Mechanics with Digital Image Correlation and Digital Volume Correlation. University of Sheffield, 2019. doi:uk.bl.ethos.781348.

[39] Barhli SM, Saucedo-Mora L, Jordan MSL, Cinar AF, Reinhard C, Mostafavi M, et al. Synchrotron X-ray characterization of crack strain fields in polygranular graphite. Carbon 2017;124:357–71. doi:10.1016/J.CARBON.2017.08.075.

[40] Barhli SM. Advanced quantitative analysis of crack fields, observed by 2D and 3D image correlation, volume correlation and diffraction mapping. University of Oxford, 2017.

[41] Marrow TJ, Liu D, Barhli SM, Saucedo-Mora L, Vertyagina Y, Collins DM, et al. In situ measurement of the strains within a mechanically loaded polygranular graphite. Carbon 2016;96:285–302. doi:10.1016/j.carbon.2015.09.058.

[42] Parks DM. The virtual crack extension method for nonlinear material behavior. Computer Methods in Applied Mechanics and Engineering 1977;12:353–64. doi:https://doi.org/10.1016/0045-7825(77)90023-8.

[43] Shih CF, Moran B, Nakamura T. Energy release rate along a three-dimensional crack front in a thermally stressed body. International Journal of Fracture 1986;30:79–102. doi:10.1007/BF00034019.

[44] Shih CF, Asaro RJ. Elastic-Plastic Analysis of Cracks on Bimaterial Interfaces: Part I—Small Scale Yielding. Journal of Applied Mechanics 1988;55:299–316. doi:10.1115/1.3173676.

[45] Oku T, Eto M. Relation between static and dynamic Young's modulus of nuclear graphites and carbon. Nuclear Engineering and Design 1993;143:239–43. doi:https://doi.org/10.1016/0029-5493(93)90226-Y.

[46] Marsden BJ, Hall GN, Jones AN. Graphite in Gas-Cooled Reactors☆. Reference Module in Materials Science and Materials Engineering, Elsevier; 2020. doi:https://doi.org/10.1016/B978-0-12-803581-8.00729-3.

[47] Arregui-Mena JD, Bodel W, Worth RN, Margetts L, Mummery PM. Spatial variability in the mechanical properties of Gilsocarbon. Carbon 2016;110:497–517. doi:https://doi.org/10.1016/j.carbon.2016.09.051.